Geophysical Research Letters

RESEARCH LETTER
10.1029/2022GL101965

**Key Points:**

- Seismic receiver functions image mantle transition zone discontinuities from a regional high-resolution transect across the eastern U.S
- The results are difficult to reconcile with either thermal or hydration variations alone in the transition zone
- Local hydro-thermal upwelling due to hydrated transition zone and hot return flow associated with the descending Farallon slab may exist

**Supporting Information:**

Supporting Information may be found in the online version of this article.

**Correspondence to:**

S. Liu,
sxliu@vt.edu

**Citation:**

Liu, S., King, S. D., Long, M. D., Benoit, M. H., & Aragon, J. C. (2023). Receiver function analysis reveals lateral variations in temperature and water content in the mantle transition zone beneath eastern North America. *Geophysical Research Letters*, *50*, e2022GL101965. https://doi.org/10.1029/2022GL101965

Received 2 NOV 2022
Accepted 9 JUN 2023



# Receiver Function Analysis Reveals Lateral Variations in Temperature and Water Content in the Mantle Transition Zone Beneath Eastern North America

**Shangxin Liu[1,2], Scott D. King[1], Maureen D. Long[3], Margaret H. Benoit[4], and John C. Aragon[3,5]**

[1]Department of Geosciences, Virginia Tech, Blacksburg, VA, USA, [2]Department of Geological Sciences, University of Florida, Gainesville, FL, USA, [3]Department of Earth and Planetary Sciences, Yale University, New Haven, CT, USA, [4]National Science Foundation, Alexandria, VA, USA, [5]Now at Earthquake Science Center, U.S. Geological Survey, Menlo Park, CA, USA

**Abstract** Using recently collected high-resolution seismic data along a dense linear transect across Ohio, West Virginia, and Virginia (called Mid-Atlantic Geophysical Integrative Collaboration (MAGIC) profile), we analyze P-to-S receiver functions to investigate the undulations of the mantle transition zone (MTZ) discontinuities (410- and 660-km) beneath the central Appalachian region. Our results incorporating the effects of local crustal and mantle structures suggest shallowing of both the 410- and the 660-km discontinuities from the northwest (inland) to the southeast (coast) along MAGIC profile. Hydro-thermal upwelling beneath the eastern U.S. coastal plain due to a hydrated MTZ and hot upwelling return flow associated with the descending lower mantle Farallon slab is consistent with our observations of MTZ structure considering 3D velocity heterogeneity. The inferred hydrous hot upwelling rising into the upper mantle may trigger dehydration melting atop the 410-km discontinuity, which may help to explain the presence of a low velocity upper mantle anomaly beneath the region today.

**Plain Language Summary** The dynamic and tectonic processes of passive continental margins that do not lie on plate boundaries are poorly understood compared with active continental margins. The mantle flow patterns beneath the eastern North America, a long-lived passive continental margin, are debated, due to limited local high-resolution seismic studies. Using a dense seismic array through Ohio, West Virginia, and Virginia (called MAGIC profile) with unprecedented resolution, we investigate the undulations of 410- and 660-km discontinuities (boundaries of the mantle transition zone) beneath the eastern U.S. by analyzing seismic waves that have been converted at these discontinuities. After correcting for local crustal and mantle structures, we identify positively correlated shallowing of the 410- and 660-km discontinuities from the inland to the coast, which are hard to explain by thermal heterogeneity alone. Our findings suggest the existence of hot upwelling return flow associated with the neighboring descending Farallon slab in the lower mantle beneath the eastern U.S. When this passive hot return flow rises through the hydrated transition zone into the upper mantle, dehydration melting atop 410-km discontinuity may be triggered. The buoyant melt may further rise through the upper mantle, providing a potential explanation for upper mantle velocity anomalies beneath the region.

## 1. Introduction

Extensive seismic studies on active continental margins have facilitated our understanding of mantle dynamics beneath plate boundaries (e.g., Becker, 2012, and the references therein). However, mantle dynamics and tectonic processes beneath passive continental margins remain less well understood due to limited local high-resolution seismic constraints. Eastern North America (Figure 1a) is an ideal place to study the attributes of passive continental margins, due to its long geological history and diverse tectonic features (e.g., Wagner et al., 2018). The region has experienced episodes of subduction and rifting associated with two complete cycles of supercontinent assembly and breakup (Rodinia and Pangea) over the past billion years (e.g., Nance et al., 2014). Meanwhile, complex shallow tectonic processes including lithospheric delamination and intraplate volcanism have occurred beneath the eastern U.S. (e.g., Long et al., 2021). Driven by mantle flow-induced dynamic topography changes, eastern North America has experienced local subsidence of up to ~-50 m over inland regions and uplift over coastal plains up to ~60 m during the past 3 million years (e.g., Rowley et al., 2013). While far from the plate

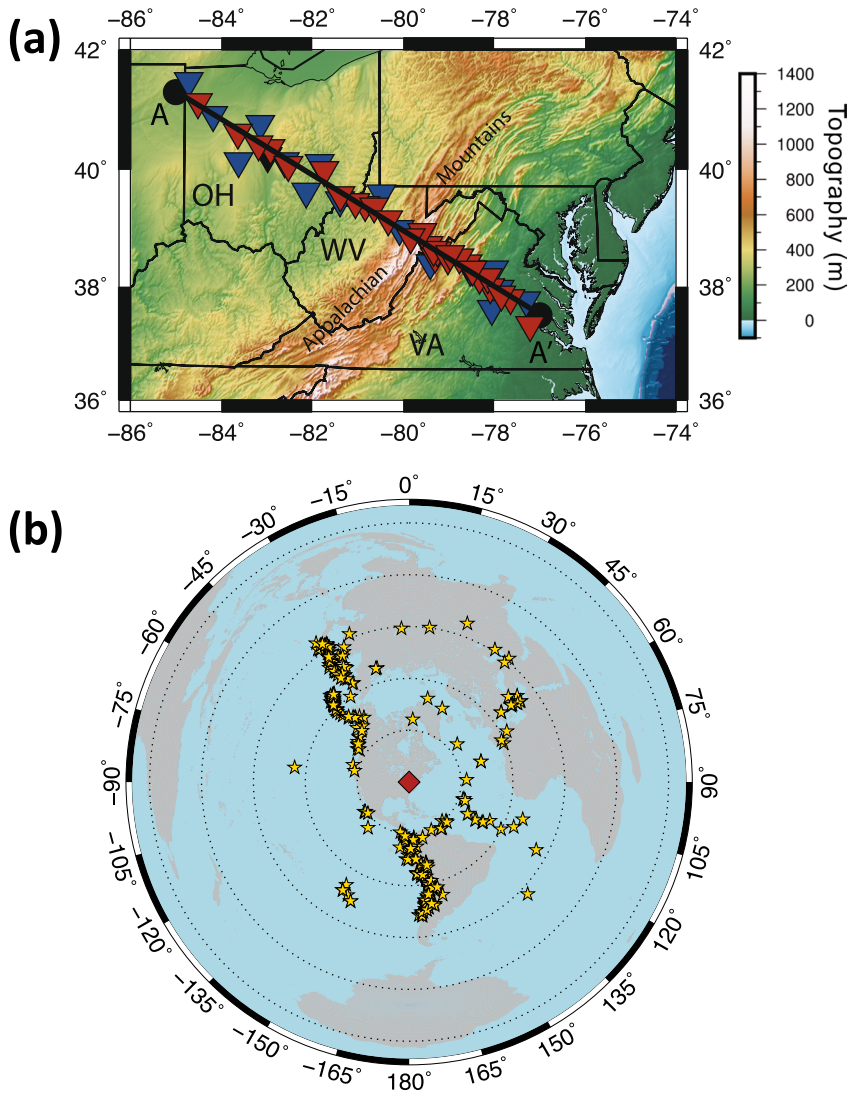


**Figure 1.** (a) Seismic stations used in this study, modified after Long et al. (2019). These include 28 MAGIC stations (red triangles), 16 neighboring TA stations (blue triangles) and 1 neighboring U.S. permanent station ACSO (black triangle). The black line marks the location of the MAGIC seismic array between two black dots, labeled A-A'. The abbreviations of three states (Ohio, West Virginia, and Virginia) and the Appalachian mountains that the MAGIC array crossed are labeled. Topography and state boundaries are also shown. (b) Map of seismic events (yellow pentagrams) used to generate RF data in this study. Red diamond denotes the location of MAGIC profile. Dotted lines show the epicentral distances at 30°, 60°, 90°, 120°, and 150°, respectively.

boundaries, active intraplate seismicity in eastern North America includes some significant large events (e.g., Neely et al., 2018; Pratt et al., 2015; Wolin et al., 2012). These intraplate earthquakes may be driven by loading stresses induced by deep mantle flow (e.g., Forte et al., 2007). Seismic anisotropy studies have identified a sharp change of the SKS splitting from NE-SW to E-W fast directions at the eastern edge of present-day Appalachian Mountains (Aragon et al., 2017). Whether and how the SKS splitting patterns relate to the deeper mantle dynamics beneath eastern North America, however, remains unknown. The complex mantle structure beneath eastern North America is characterized by the sharp eastern edge of North American cratonic keel (e.g., Schmandt & Lin, 2014), a small region of missing lithospheric mantle below the central West Virginia/Virginia (WV/VA) border (e.g., Biryol et al., 2016; Schmandt & Lin, 2014; Wagner et al., 2018), and the Farallon slab in the lower mantle (e.g., Grand, 2002). The missing lithospheric mantle may indicate the existence of a delaminated or dripped dense lithospheric blocks due to a Rayleigh-Taylor instability (Conrad & Molnar, 1997; Göğüş &

Pysklywec, 2008). The same region has the prominent record of past magmatic activities (Mazza et al., 2014) and the partial melt may be still present in the underlying upper mantle today (e.g., Evans et al., 2019).

Three possible dynamic scenarios that invoke vertical mantle flow beneath eastern North America, which may cause undulations of the 410- and 660-km phase transition boundaries (e.g., Shearer, 2000), have been previously suggested for the region. One possible scenario is that the sharp craton edge generates small-scale convection, with a cold downwelling limb beneath the eastern U.S. craton boundary (King & Anderson, 1998). King (2007) showed that the corresponding hot upwelling limb of such small-scale convection could explain the formation of Bermuda hotspot (see also Benoit et al., 2013). A thicker mantle transition zone (MTZ), with an elevated 410-km discontinuity and a slightly depressed 660-km discontinuity beneath the edge of the eastern North America craton root, would be consistent with the cold downwelling mantle flow (Bina & Helffrich, 1994). The second idea proposes a widely distributed, hydrous upwelling along the eastern North American continental margin, as inferred from the slow shear wave velocity in the upper mantle from regional seismic tomography (van der Lee et al., 2008). The proposed source of the volatiles is the dehydration of the Farallon slab near the top of the lower mantle, where dense hydrous magnesium silicates break down (e.g., Komabayashi et al., 2004). Hydration lowers the pressures for the olivine to wadsleyite phase transformation at the 410-km discontinuity (e.g., Ohtani & Litasov, 2006; Smyth & Frost, 2002; Wood, 1995) and increases the pressures for the ringwoodite to bridgmanite phase transformation at the 660-km discontinuity (e.g., Higo et al., 2001; Ohtani & Litasov, 2006), with the former being more strongly affected than the latter. Therefore, with an elevated 410-km discontinuity and a slightly deepened 660-km discontinuity, a hydrous MTZ is expected to be thicker than anhydrous one. The third idea involves the missing lithospheric mantle below the central WV/VA border, which is clearly observed by recent seismic tomography (e.g., Biryol et al., 2016; Schmandt et al., 2015; Schmandt & Lin, 2014; Shen & Ritzwoller, 2016; Wagner et al., 2018) and is also suggested by other observations (Evans et al., 2019; Long et al., 2021). The potential location of this hypothesized delaminated or dripped lithospheric block in the deeper mantle has not been clearly identified yet. If a cold lithospheric block resides in the MTZ, we would expect a localized shallower 410-km discontinuity or deeper 660-km discontinuity, which would thicken the MTZ, beneath a small segment of eastern North America (Bina & Helffrich, 1994). Although all of these three potential scenarios would suggest a thicker MTZ beneath the eastern U.S., the vertical coherence of the effects of these three processes to the MTZ topography may be different. For instance, a delaminated lithospheric block may not affect the 410- and 660-km discontinuities below the same location if its size is small or the sinking does not follow an exactly vertical trajectory, different from the effects of a downwelling limb of the edge-driven convection and vertical transport of volatiles. Investigations of MTZ structure may be used to reveal the possible presence of vertical mantle flow and discriminate among different dynamic processes.

The Mid-Atlantic Geophysical Integrative Collaboration (MAGIC) project provides an opportunity to image mid mantle structure throughout the Appalachian region of the eastern U.S. in unprecedented detail. The project deployed 28 broadband seismometers in a dense linear transect across Ohio, West Virginia, and Virginia, running through the year 2013–2016, with most stations operating for 24 months (Long et al., 2020). Combined with the neighboring EarthScope USArray Transportable Array (TA) stations, a high-resolution seismic profile extending from the continental interior to the Atlantic coast beneath the eastern U.S. can be formed (Figure 1a), achieving a nominal station spacing of ∼25 km, compared with the nominal spacing of ∼70 km for only TA stations. We use P-to-S (Pds) receiver functions (RFs) (e.g., Langston, 1977; Vinnik, 1977) to investigate the geometries of the MTZ discontinuities (410- and 660-km boundaries) beneath the MAGIC array, which may constrain the vertical mantle flow patterns beneath the eastern U.S.

## 2. Receiver Functions

### 2.1. Method

The details of the data collection for the MAGIC array can be found in Long et al. (2020). Sixteen neighboring TA stations, mostly operating between 2012 and 2015, and one U.S. permanent station are also used to improve the resolution (Figure 1a). We use the software Funclab (Eagar & Fouch, 2012; Porritt & Miller, 2018) to request and process the seismic data. We select among all the earthquakes with moment magnitudes larger than 6.0 between the epicentral distances of 30° and 100° occurring during the operation time of each station, as shown in Figure 1b. After rotating the seismograms from the original ENZ coordinate system into the RTZ coordinate system, the waveforms are band-pass filtered between 0.15 and 5.0 Hz, and the RFs are computed using a time

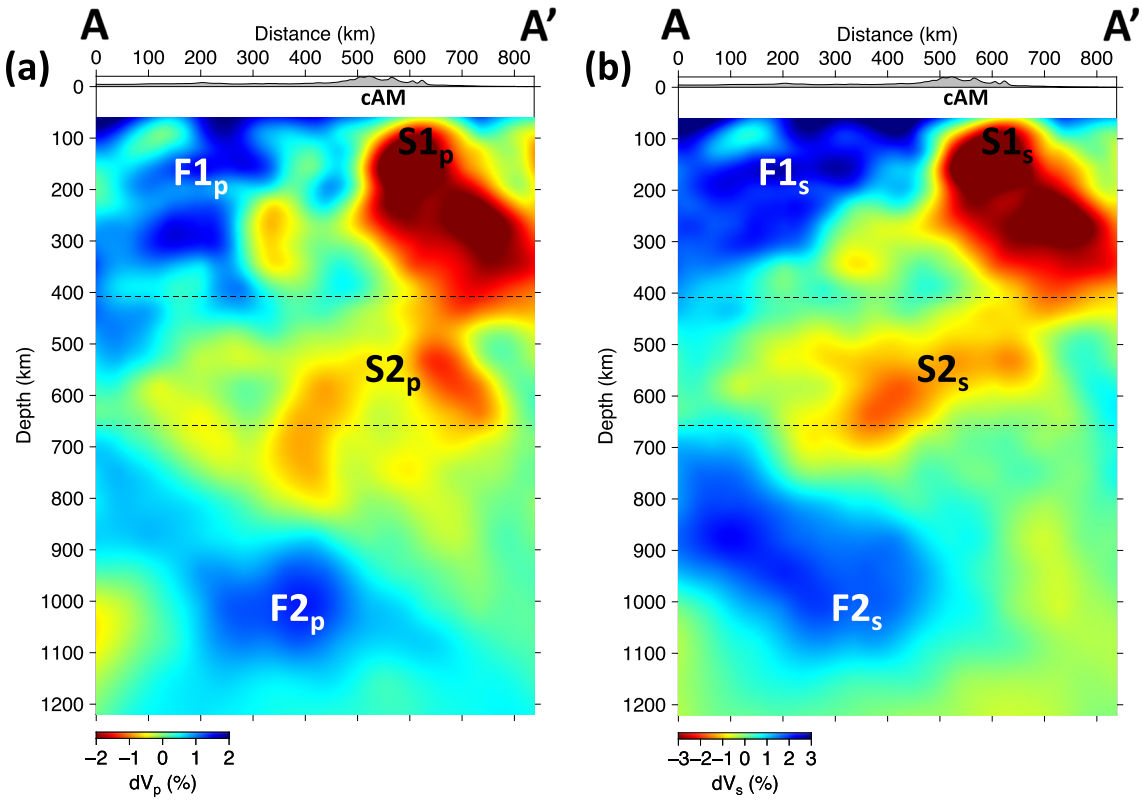


**Figure 2.** Vertical cross sections through the SL14 (a) P wave tomographic model and (b) S wave tomographic model of the mantle beneath the U.S. from Schmandt and Lin (2014) along MAGIC profile labeled A-A' in Figure 1a. Local surface topography (km X20) along the profile is indicated, with the location of central Appalachian Mountains (cAM) identified. The horizontal black dashed lines mark the depths of MTZ boundaries at 410- and 660-km, respectively. The color scale is over-saturated in the top part of the upper mantle in order to highlight the deeper mantle velocity anomalies with smaller amplitudes. The upper mantle includes the inland high-velocity North American cratonic root ($F1_p/F1_s$) to the northwest and the slow-velocity missing lithospheric mantle ($S1_p/S1_s$) to the southeast, close to the coast. The slow-velocity anomalies in the MTZ ($S2_p/S2_s$) indicate the potential thermal or hydrous upwelling. The lower mantle is featured with high-velocity Farallon slab remnants ($F2_p/F2_s$).

domain iterative deconvolution approach (Ligorria & Ammon, 1999) to deconvolve the vertical from the radial components with a Gaussian width parameter ("a" value) of 1.0. We also experiment with a Gaussian width parameter of 0.6 and find that it yields very similar results. We visually inspect all the RFs for each station, rejecting RFs that lack a clear first P arrival with correct timing and polarity. RFs with large negative troughs directly preceding or following the first P arrival and RFs with excessive harmonic oscillation or anomalous large spurious peaks are also removed. A significant number of the traces have strong harmonic oscillation due to the large velocity contrasts caused by sedimentary accumulation within the crust (e.g., Cook & Vasudevan, 2006), consistent with the finding from previous RF study below eastern North America (e.g., Long et al., 2010), and we have to abandon a relatively large volume of poor quality data. The average number of high-quality RFs per station used for single-station and 2D CCP stacking is 35.

The RFs are first migrated to depth using the 1D AK135 radial seismic velocity reference model (B. L. N. Kennett et al., 1995). Corrections for the effects of 3D velocity structure are further performed using SL14 crustal and mantle seismic tomographic models beneath the U.S. from Schmandt and Lin (2014). Because the mantle seismic tomographic model is inverted based on an initial crustal seismic tomographic model in Schmandt and Lin (2014), we use the same crustal model to perform the 3D corrections, along with the mantle model, to make our 3D corrections consistent with SL14 models. The mantle seismic tomography from SL14 models below the MAGIC profile, which exhibits complex lateral heterogeneity, is shown in Figure 2. To investigate the robustness of the lateral velocity heterogeneity revealed by SL14 models and the resulting 3D velocity corrections, we compare the P wave velocity perturbations from SL14 models below the MAGIC profile with those imaged by another two recent P wave tomography models, BBNAP19 (Boyce et al., 2019) and Liang et al. (2022), as shown in Figure S1 in Supporting Information S1. S wave velocity perturbations below the MAGIC profile are also compared with

another three recent S wave tomography models, MITS18 (Golos et al., 2018), SAVANI-US (Porritt et al., 2021) and NASEM5 (Clouzet et al., 2018), as shown in Figure S2 in Supporting Information S1. All the seismic models presented for comparisons use all the TA stations across the U.S. Although there are a certain degree of differences on the amplitudes and the geometries of the prominent velocity anomalies in the mantle due to different seismic data and inversion methods used in these studies (such as damping, smoothing, and wavelength filtering), the first-order velocity structures below the MAGIC profile between different models are similar (see Figures S1 and S2 in Supporting Information S1). We do not make topographic corrections, because the influence of the elevation variations across our seismic profile on the arrival time of the RFs is negligible (see Text S1 and Table S1 in Supporting Information S1). Single-station stacking of the radial RFs along the profile is performed across all backazimuths and epicentral distances for each station. Because the lateral move-out of RFs at transition zone depths are much more significant than at lithosphere depths, we caution that the single-station stacking results are simply a reflection of a broad average of the mantle structure below each station. The depths of the 410- and 660-km boundaries are picked and the average thickness of the MTZ below each station is calculated. The dense seismic profile (~15 km station spacing at its densest portion) also enables us to construct a high-resolution seismic image using the common conversion point (CCP) stacking method (Dueker & Sheehan, 1997). Because the 410- and 660-km piercing points are distributed closely along our profile (see Text S2 and Figure S3 in Supporting Information S1), we elect to perform 2D CCP stacking along our profile, that is, the conversion points produced by the impedance contrasts or gradients on the raypaths are projected onto a transect plane. Based on the distribution of the piercing points, the 2D CCP stacking is performed throughout three regions (black, brown, and magenta rectangular boxes in Figure S3 in Supporting Information S1). Black rectangular box centering around the MAGIC profile A-A' defines the piercing points within 3-degree range perpendicular to the MAGIC profile that are used for the "total 2D CCP stacking." Brown rectangular box centering around the neighboring parallel profile B-B' defines the piercing points within 1-degree range perpendicular to the profile B-B' that are used for the "north-side partial 2D CCP stacking." Magenta rectangular box centering around the neighboring parallel profile C-C' defines the piercing points within 1.5-degree range perpendicular to the profile C-C' that are used for the "south-side partial 2D CCP stacking." Note that the 660-km piercing points show poor coverage within the area close to the coastal end of the B-B' rectangular box and the area close to the inland end of the C-C' rectangular box (see Figure S3 in Supporting Information S1). Therefore, the north-side partial 2D CCP stacking along B-B' does not calculate the 660-km discontinuity depth and the MTZ thickness close to the coastal end B'; the south-side partial 2D CCP stacking along C-C' does not calculate the 660-km discontinuity depth and the MTZ thickness close to the inland end C (see Figure S4 in Supporting Information S1 and Figure 3). The results of the MTZ discontinuities produced without and with the 3D velocity corrections are both presented to clearly show the effects of the 3D mantle structure on our estimates of MTZ discontinuity depths.

### 2.2. Results

Figure S4 in Supporting Information S1 shows both single-station stacking results and 2D CCP stacking results (using 70-km horizontal and 2-km vertical bin sizes) along MAGIC transect calculated from the 1D AK135 velocity model. The 410- and 660-km discontinuity depths in Figures S4a and S4b in Supporting Information S1 are picked from the original RF traces of single-station stacking (Figure S5 in Supporting Information S1) and the 2D CCP stacking images (Figure S7 in Supporting Information S1 for total 2D CCP stacking). The general trends of the results from the two methods are consistent along the profile. The 410-km discontinuities from north-side partial 2D CCP stacking, south-side partial 2D CCP stacking, and total 2D CCP stacking are very close along the profile, indicating that the neighboring lateral change of the upper mantle structures perpendicular to the MAGIC profile is small. The depths of 660-km discontinuities and hence the MTZ thickness from the two partial 2D CCP stacking results show a prominent discrepancy below the middle part of the MAGIC profile (within 300–500 km from the northwestern end of the MAGIC profile), which indicates a local significant lateral perturbation of the mantle structure perpendicular to the MAGIC profile. However, except for the areas with sparse distribution of the 660-km piercing points (see Figure S3 in Supporting Information S1), the trends of the three 2D CCP stacking results are highly consistent along the MAGIC profile. From the continental interior to the Atlantic coast, both the 410-km discontinuity (Figure S4a in Supporting Information S1) and the 660-km discontinuity (Figure S4b in Supporting Information S1) are generally flat, with a relatively abrupt deepening of ~10 km moving to the southeast (around ~500 km from the northwestern end of the MAGIC profile) beneath the Appalachian mountains (a two-step shape). This sharp transition may be due to the fact that the Pds arrival

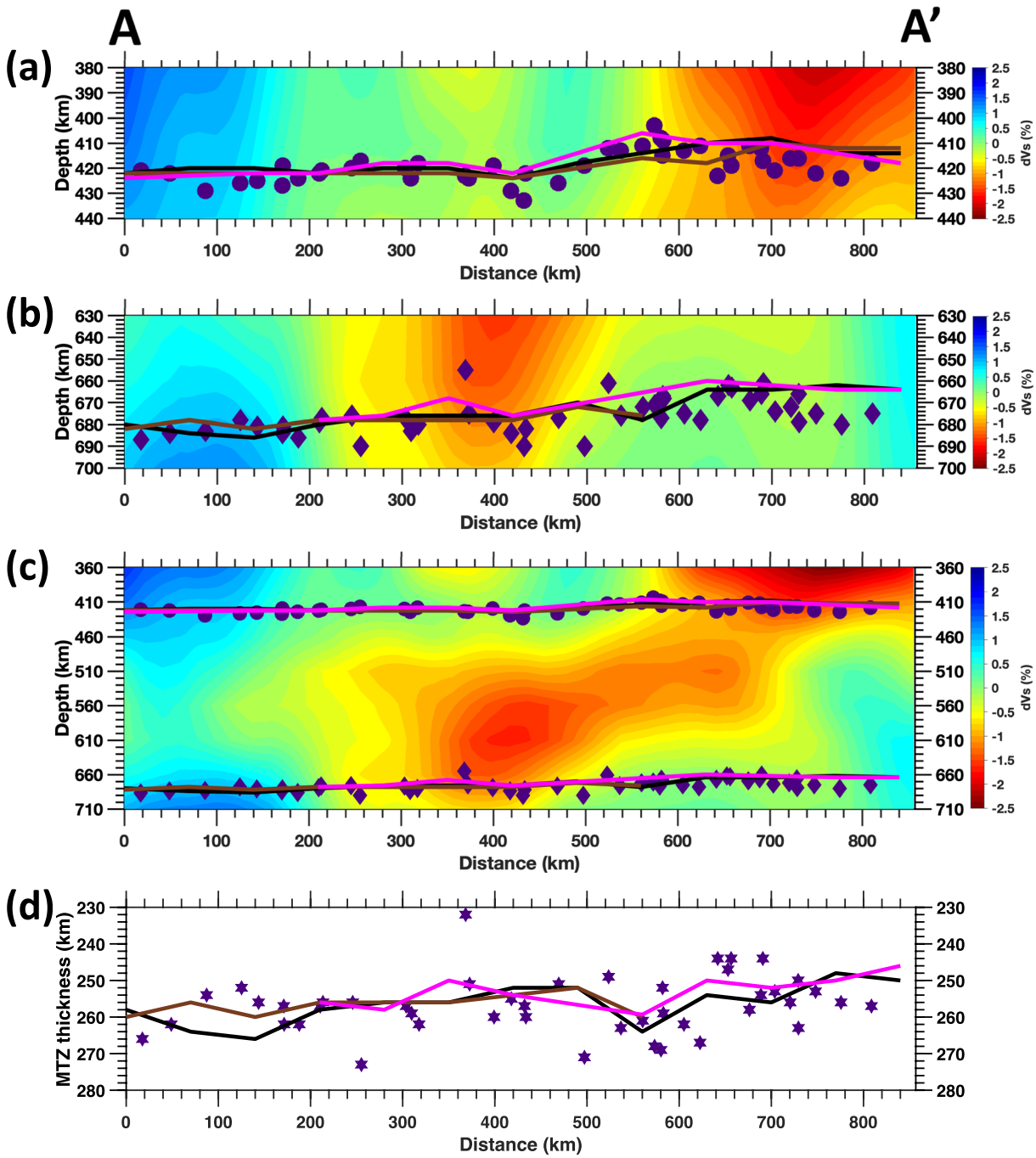


**Figure 3.** (a) 410-km discontinuity depth, (b) 660-km discontinuity depth, (c) 410- and 660-km discontinuity depths, and (d) MTZ thickness calculated from 1D AK135 radial velocity model with the 3D corrections using the crustal and mantle seismic tomographic models from Schmandt and Lin (2014) along the MAGIC profile labeled A-A' in Figure 1a. Scattered indigo points denote single-station stacking results (410-km: circle; 660-km: diamond; MTZ thickness: hexagram). Black solid lines denote total 2D CCP stacking results defined by the black rectangular box in Figure S3 in Supporting Information S1. Brown solid lines denote north-side partial 2D CCP stacking results defined by the brown rectangular box in Figure S3 in Supporting Information S1. Magenta solid lines denote south-side partial 2D CCP stacking results defined by the magenta rectangular box in Figure S3 in Supporting Information S1. The background in top three panels depicts the shear velocity structure from the seismic tomographic model of Schmandt and Lin (2014). The results we show here use this velocity model for 3D corrections.

time is affected by the local upper mantle structure, with a slow velocity anomaly beneath the southeastern part and fast velocities beneath the northwestern part (see Figure 2), but the velocity model assumes a simple 1-D profile. Correspondingly, the MTZ thickness is generally uniform from the continental interior to the Atlantic coast (Figure S4d in Supporting Information S1). Because the sharp transition in the stacking results of 410-km

(Figure S4a in Supporting Information S1) and 660-km (Figure S4b in Supporting Information S1) discontinuities is located around ~500 km from the northwestern end, we divide the whole profile into a northwestern segment and a southeastern segment bounded by the horizontal distance of 500 km from the northwestern (inland) end of the profile. We then calculate the average 410-km depth, 660-km depth, and MTZ thickness from both single-station stacking and total 2D CCP stacking below the whole profile, northwestern segment, and the southeastern segment, respectively, as shown in Table S2 in Supporting Information S1. The results of average statistics from single-station stacking are nearly the same as those from total 2D CCP stacking, consistent with Figure S4 in Supporting Information S1. The average statistics in Table S2 in Supporting Information S1 also clearly demonstrate a two-step shape, with a ~10 km jump of the 410- and 660-km discontinuities along MAGIC profile (Figure S4 in Supporting Information S1).

Using the same data and technical parameters as those in 1D stacking, we next calculate both single-station stacking and 2D CCP stacking along the MAGIC transect from the 1D AK135 radial velocity model with 3D corrections applied using the SL14 crustal and mantle seismic tomographic models from Schmandt and Lin (2014) (Figure 3). The single-station stacking considering the 3D velocity corrections uses a modified reference 1D velocity profile interpolated from SL14 models below each station to perform the trace stacking. The 410- and 660-km discontinuity depths in Figure 3 are picked from the original RF traces of single-station stacking (Figure S6 in Supporting Information S1) and the images of 2D CCP stacking (Figure S8 in Supporting Information S1 for total 2D CCP stacking). The distributions of the 410-km discontinuity, 660-km discontinuity, and MTZ thickness from single-station stacking with 3D velocity corrections (Figure 3) are more variable with depth than the 1D single-station stacking results (Figure S4 in Supporting Information S1), which reflects the larger variations of the RFs from different back azimuths for each station when using the 3D models. However, the general trends from the single-station stacking results with 3D velocity corrections are still clear, and are consistent with the 2D CCP stacking results (Figure 3). Except for the areas with sparse distribution of the 660-km piercing points (see Figure S3 in Supporting Information S1), the 410-km discontinuities, 660-km discontinuities, and the MTZ thickness from north-side partial 2D CCP stacking, south-side partial 2D CCP stacking, and total 2D CCP stacking are all very close along the profile. The prominent discrepancy between the 660-km depths and the MTZ thickness from the two partial 2D CCP stacking results below the middle part of the MAGIC profile (within 300–500 km from the northwestern end of the MAGIC profile) disappears with the consideration of the 3D velocity corrections, which confirms the existence of the significant lateral perturbation of the mantle structures beneath this region and the necessity of the 3D velocity corrections for the 2D CCP stacking. When the 3D velocity corrections are incorporated into our estimates, we find that, both the 410-km (Figures 3a) and 660-km (Figure 3b) discontinuities smoothly shallow from the continental interior to the Atlantic coast. Specifically, the 410-km discontinuity shallows by ~10–15 km from the inland plain to the coastal plain, while the 660-km discontinuity shallows by ~20–25 km. Because the 660-km discontinuity (Figure 3b) has a slightly steeper slope than the 410-km discontinuity (Figure 3a), the MTZ thickness modestly decreases by ~5–10 km along the profile (Figure 3d).

The considerable differences in the trends of the MTZ discontinuities between the results with and without the 3D velocity corrections are a result of the strong lateral seismic velocity perturbations in the upper mantle and MTZ beneath the MAGIC array (Figure 2). In the upper mantle, these velocity perturbations include a fast anomaly to the northwest beneath the inland part of the MAGIC array ($F1_p/F1_s$) and a slow anomaly to the southeast below central Appalachian Mountains ($S1_p/S1_s$). The slow anomaly in the MTZ ($S2_p/S2_s$) is another significant lateral velocity perturbation that is important for our estimates of the 660-km discontinuity depth. Our results indicate that the 3D velocity anomalies significantly alter estimates of the undulations of the 410- and 660-km boundaries beneath eastern North America. Because the results from north-side partial 2D CCP stacking, south-side partial 2D CCP stacking, and total 2D CCP stacking are very similar, the analyses of the 2D CCP stacking below are based on total 2D CCP stacking.

## 3. Discussion

### 3.1. Analysis of the Results From 1D Stacking

In spite of the large variation in crust and lithospheric structures across the MAGIC profile from the northwestern end (western Ohio) to the southeastern end (eastern Virginia) (Long et al., 2020, 2021), the underlying upper boundary of the MTZ, that is, 410-km discontinuity, is relatively smooth, with a deepening of ~10 km

moving to the southeast (around ~500 km from the northwestern end of the MAGIC profile) beneath Appalachian mountains (Figure S4a in Supporting Information S1). Similarly, the 660-km discontinuity also exhibits a two-step shape, with a deepening of ~10 km to the southeast (around ~500 km from the northwestern end of the MAGIC profile) beneath Appalachian mountains (Figure S4b in Supporting Information S1). The trend of our 1D stacked 410-km discontinuity from the inland to the coast beneath the eastern U.S. (Figure S4a in Supporting Information S1) shows good agreement with the 1D P-to-S stacked results beneath contiguous U.S. from Gao and Liu (2014), who uses the IASP91 radial profile (B. Kennett & Engdahl, 1991) as the reference velocity model. In contrast, the 660-km discontinuity along the MAGIC profile interpolated from Gao and Liu (2014) largely stays flat at ~660 km and does not show the two-step shape in our 1D stacked results (Figure S4b in Supporting Information S1).

Because we are not accounting for 3D crustal and upper mantle structures, and because the 1D velocity model may be imperfect for the region, the 410- and 660-km discontinuities are apparent rather than true depths. We calculate the difference between the two discontinuity depths to yield an estimated MTZ thickness profile beneath the MAGIC array, as shown in Figure S4d in Supporting Information S1. Because both the 410- and 660-km discontinuities are nearly identically affected by lateral velocity variations in crustal and upper mantle structures, the differencing of depths (i.e., MTZ thickness) yields a more accurate result than the individual depths. In spite of the two-step shapes in the 410- and 660-km discontinuity depths, the MTZ thickness is largely uniform across the entire profile (Figure S4d in Supporting Information S1). A local slight thickening occurs around 550 km from the northwestern end of the profile beneath Appalachian mountains, but this thickening is slight and does not exceed 10 km. The average MTZ thickness across the profile is ~258 km (see Table S2 in Supporting Information S1), which is thicker than the global 1D stacked value of ~247.4 km (Lawrence & Shearer, 2006) and the regional 1D stacked value of ~244.2 km across the southeastern North America from local permanent broadband seismic stations (Long et al., 2010), but is close to the average 1D stacked MTZ thickness of ~251 km across the whole central and eastern U.S. (east of 102°W) (Gao & Liu, 2014). The generally uniform trend, with no obvious thickening of the MTZ along the MAGIC profile, would seem to be inconsistent with the presence of edge-driven convection, a hydrous upwelling, or a delaminated or dripped cold lithospheric block beneath the coastal plain, all of which would predict a region of local MTZ thickening.

### 3.2. Analysis on the Results From 3D Stacking

Given the significant velocity perturbations in the crust and upper mantle beneath eastern North America (Figure 2), we now consider the results using the 1D AK135 radial velocity model with the 3D velocity corrections (Schmandt & Lin, 2014), as shown in Figure 3. These estimates account for lateral velocity variations in the crust, the upper mantle, and the MTZ itself, although there are some uncertainties in the models used to make the corrections. Figure 2 shows that the MTZ beneath the middle to southeastern part of the MAGIC profile includes a large patch of slow seismic velocity ($S2_p/S2_s$), which could indicate either anomalously warm mantle or a hydrous zone. Because the single-station stacking results using 3D corrections show a relatively large variability (Figure 3), we mainly rely on our 2D CCP stacking results (Figure 3) to analyze the corresponding dynamic implications. With the 3D velocity corrections, both the 410- and 660-km discontinuities gradually shallow from the northwestern end (western Ohio) to the southeastern end (eastern Virginia) of the profile (Figure 3). The significant differences of the 410- and 660-km trends between the results with and without the 3D corrections are primarily caused by the strong lateral seismic velocity contrasts in the upper mantle associated with the cratonic root to the northwest beneath the inland part of the MAGIC array ($F1_p/F1_s$ in Figure 2) and the missing lithospheric mantle to the southeast below central Appalachian Mountains below the MAGIC profile ($S1_p/S1_s$ in Figure 2).

There are several previous P-to-S receiver function results for the MTZ beneath the eastern U.S. from 3D stacking (e.g., Gao & Liu, 2014; Y. Wang & Pavlis, 2016; Maguire et al., 2018; Keifer & Dueker, 2019). Among these models, we compare our local 410- and 660-km depths from 3D stacking with those from Maguire et al. (2018), who also used the seismic tomographic models from Schmandt and Lin (2014) for 3D velocity corrections. The results from Maguire et al. (2018) have an average 410-km discontinuity at 412 km depth and an average 660-km discontinuity at 663 km depth across the whole central and eastern U.S. The average depths of 410- and 660-km discontinuities beneath the MAGIC profile from our 2D CCP stacking results are 417- and 674-km, respectively. They are both deeper than their corresponding background average values, which is consistent with the

results from Maguire et al. (2018) below Ohio, West Virginia, and Virginia. Our deeper 410-km discontinuity may suggest that the upper mantle beneath the MAGIC profile is hotter than the background mantle beneath the central and eastern U.S. as a whole, while our deeper 660-km may suggest that the lower MTZ beneath the MAGIC profile is either colder or more hydrous than the regional background mantle. The broader-scale result along the MAGIC profile interpolated from Maguire et al. (2018) features a shallowing trend of the 410-km discontinuity below the coastal plain, which is consistent with our result (Figure 3a). In contrast, the 660-km discontinuity along the MAGIC profile interpolated from Maguire et al. (2018) is nearly flat, different from the shallowing trend in our result (Figure 3b). In our images, the shallowing trend of 410-km interface from the inland to the coast could be consistent with the thermal blanketing effect of cratonic lithosphere due to the warmer upper mantle beneath the inland cratonic root (Grigné & Labrosse, 2001). The shallower 410-km interface beneath the coastal plain also seemingly supports the edge-driven convection (King & Anderson, 1998) and hydrous upwelling (van der Lee et al., 2008) ideas; however, the same shallower underlying 660-km interface contradicts these two mantle dynamic scenarios. The shallower 410-km discontinuity below the southeastern part of the MAGIC profile (Figure 3a) could possibly support the scenario that a delaminated or dripped cold lithospheric block beneath northern Virginia is sinking into the MTZ from the upper mantle (Bina & Helffrich, 1994), but this would also result in a locally thicker MTZ.

We calculate the MTZ thickness with the 3D velocity corrections, as shown in Figure 3d. In contrast to the largely uniform MTZ thickness trend from the 1D stacking, the MTZ thickness from the 3D stacking decreases somewhat from the inland to the coast, although the thickness variation across the whole profile does not exceed 10 km. At the southeastern end of the profile, beneath the coastal plain, the MTZ thickness is around 250 km, slightly thicker than the global average values of ∼241–243 km (Flanagan & Shearer, 1998; Gu et al., 1998; Lawrence & Shearer, 2006) from 3D stacking but close to the average values of the MTZ thickness of ∼251 km across the whole central and eastern U.S. from the 3D stacking (Maguire et al., 2018). At the northwestern end of the profile, below the inland plain, the MTZ thickness is around 260 km, thicker than the global average and the average across the whole central and eastern U.S.

The thinner MTZ below the coastal plain of the eastern U.S. is obviously not consistent with either the edge-driven convection (King & Anderson, 1998) or the presence of a delaminated or dripped cold lithospheric block trapped in the MTZ below northern Virginia. In the context of the hydrous upwelling scenario, the slight thinning trend of the MTZ thickness from the inland to the coast could suggest that the MTZ below the continental interior is somewhat more hydrated (and therefore has a thicker MTZ) than the MTZ below the coastal plain. This is inconsistent with the speculation in van der Lee et al. (2008) that the hydrous upwelling is located below the U.S. east coast. However, the recent regional mantle seismic tomographic model below the eastern U.S. (Figure 2) shows that the top lower mantle portion of the Farallon slab ($F2_p$/$F2_s$) is located below the inland (northwestern) part of the MAGIC profile. In this scenario, the upward transport of volatiles from the dehydration of the Farallon slab at the top of the lower mantle could indeed primarily hydrate the MTZ right beneath the inland cratonic root, which is consistent with a thicker MTZ. The accurate mapping of the location of the Farallon slab in the mid-mantle is a key to determine the location of the potentially water-saturated MTZ below the eastern U.S. The recent mantle seismic tomographic model (Schmandt & Lin, 2014) indicates that the major hydrated part of the MTZ below the eastern U.S. associated with the dehydration of the underlying Farallon slab may actually locate below the continental interior, instead of the coastal plain. Although we suggest that the MTZ below the continental interior may potentially be hydrated, it is notable that a hydration-induced ∼10 km thickening of the MTZ is smaller than what would be expected for a water-saturated MTZ (Smyth & Frost, 2002). The hydration indicated by van der Lee et al. (2008) would produce ∼20–40 km of MTZ thickening if the effect is entirely due to the elevation of the 410-km discontinuity under water-saturated conditions (Smyth & Frost, 2002). A ∼10 km thickening of the MTZ below the inland portion of the MAGIC array indicates the hydrous upwelling below this region, if present alone, is weaker than that suggested by the mechanism proposed by van der Lee et al. (2008).

### 3.3. Hydro-Thermal Upwelling Mechanism

While a more hydrated MTZ beneath the northwestern portion of our profile may potentially explain the relatively (slightly) thicker MTZ there, it does not provide a good explanation for the simultaneous shallowing of both the 410- and 660-km discontinuities to the southeast along our profile. These results also cannot be reconciled with thermal effects alone, although the broader-scale MTZ topography across the central and eastern U.S. may

be primarily attributed to the thermal variations (Keifer & Dueker, 2019). Therefore, we seek a conceptual mantle dynamic model that can explain our local smaller-scale observations, along with the velocity structures shown in Figure 2. The widespread slow velocity anomaly within the MTZ beneath the middle to southeastern part of the MAGIC profile ($S2_p$ and $S2_s$ in Figures 2a and 2b, respectively), which produces a thinner MTZ below the coastal plain, is somewhat puzzling. A hydrous upwelling alone cannot explain this prominent slow velocity anomaly because that scenario would predict a thicker, rather than a thinner, MTZ below the coastal plain. Moreover, the P wave mantle seismic tomography (Figure 2a), which is typically better-resolved than S wave mantle seismic tomography (Figure 2b), identifies two distinct low velocity volumes in this location ($S2_p$). The slow velocity anomaly toward the inland (northwestern) direction is located right above the underlying top lower mantle portion of the Farallon slab ($F2_p$) whereas the slow velocity anomaly toward the coast (southeastern) direction is located right below the widespread slow velocity anomaly in the upper mantle ($S1_p$). The slow velocity anomaly toward the northwest may represent the hydrous upwelling from the dehydration of the Farallon slab near the top of the lower mantle. However, in the context of a thinner MTZ below the coastal plain, the slow velocity anomaly to the southeast may indicate a high temperature perturbation within the MTZ below the southeastern segment of the MAGIC profile.

The origin of this presumably hot anomaly needs further investigation. We suggest that this hot anomaly may be produced by hot return flow from a super-adiabatic lower mantle (Khan et al., 2006; Verhoeven et al., 2009) induced by the neighboring sinking Farallon slab ($F2_p$/$F2_s$), as illustrated in Figure 4. This passive upward poloidal return flow induced by the sinking of the Farallon slab may be enhanced with the decrease of the slab-to-mantle viscosity ratio (Piromallo et al., 2006). Figure 2 shows a small-amplitude slow velocity anomaly adjacent to the Farallon slab in the lower mantle below the southeastern part of the profile, which may correspond to our hypothesized passive hot return flow (Figure 4). Because the sinking slab and the induced passive hot return flow align closely to each other (Piromallo et al., 2006), seismic tomography imaging may obscure the geometry and magnitude of the passive hot upwelling adjacent to the sinking slab.

In the context of this idea, the elevated 660-km discontinuity along the southeastern part of the MAGIC profile can be explained by hot upwelling return flow from the lower mantle rising up into the MTZ (Figure 4). As the hot upwelling rises through the hydrated MTZ fed by the dehydration of the Farallon slab at the top of the lower mantle, its high water content will induce a relatively shallower 410-km discontinuity beneath the coastal plain (Figure 4). When the hydrated hot upwelling passes through the 410-km discontinuity, the transformation of wet wadsleyite to dry olivine may release water to trigger partial melting above the discontinuity, as proposed by the MTZ water filter hypothesis (Bercovici & Karato, 2003; Leahy & Bercovici, 2007). Evidence for a dehydration melting layer atop the hydrated MTZ has been reported in the regions where mantle flow rises through the 410-km discontinuity (e.g., X.-C. Wang et al., 2015; Wei & Shearer, 2017). The melt may further ascend through the upper mantle (Figure 4) if it is positively buoyant, which would be consistent with the prominent slow velocity anomaly within the upper mantle beneath the coastal plain ($S1_p$/$S1_s$). The dehydration-induced melt could reach the base of the lithosphere, as shown in Figure 4, potentially explaining the presence of partial melt in the upper mantle today (Byrnes et al., 2019; Evans et al., 2019; Long et al., 2021).

A local hot mantle upwelling generated by subduction-triggered return flow has been adopted to explain the intraplate magmatism and volcanism in other regions (e.g., Faccenna et al., 2010; Zhou, 2018). Global finite-frequency tomography of the 410- and 660-km discontinuities have revealed a strong positive correlation between 410- and 660-km discontinuities (both are deeper) under major subduction zones, suggesting the possible widespread distribution of the hot return flow from the lower mantle warming up the shallow MTZ above the cold stagnant slabs (Guo & Zhou, 2021).

## 4. Conclusions

Seismic data along the MAGIC profile enables us to constrain the depths of the 410- and 660-km discontinuities, along with MTZ thickness, beneath the eastern U.S. with unprecedented high resolution. Using the AK135 reference radial velocity profile, our 1D stacking yields a largely uniform trend of the MTZ thickness across the MAGIC profile, generally consistent with previous broader-scale 1D stacked results from TA (Gao & Liu, 2014) and permanent (Long et al., 2010) seismic stations with sparser data coverage beneath the eastern U.S. There are significant differences in the trends of the 410-km discontinuity, 660-km discontinuity, and MTZ thickness along the MAGIC profile between the results without and with 3D seismic velocity corrections, which indicates the

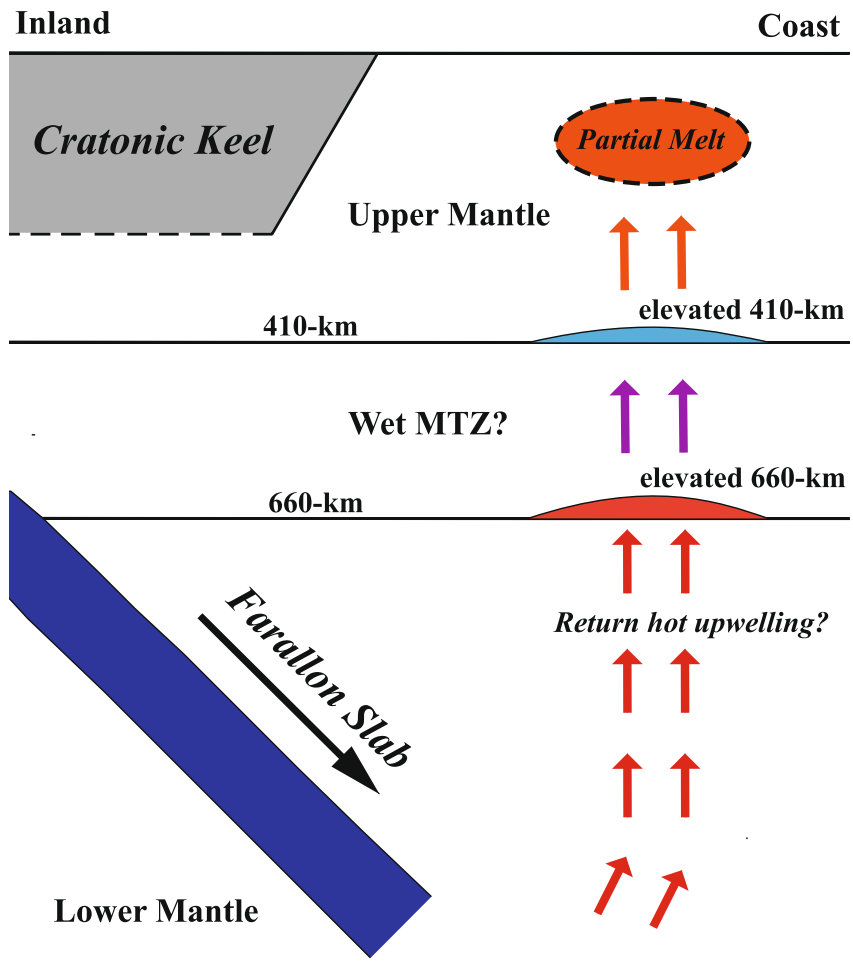


**Figure 4.** A schematic cartoon (not to scale) illustrating a possible hydro-thermal upwelling mechanism below the eastern U.S. The blue feature in the lower mantle represents the cold downwelling associated with the subduction of the Farallon slab. Red arrows in the lower mantle represent possible hot upwelling return flow induced by the subduction of the neighboring Farallon slab. Purple arrows represent the hydrated hot upwelling in the wet MTZ between 660-km discontinuity and 410-km discontinuity. Orange arrows in the upper mantle represent the possible rising positively buoyant melt after the dehydration melting of the hydro-thermal upwelling atop 410-km discontinuity. There are considerable uncertainties about the lateral and depth extents of the shallow partial melt region, as indicated by the dashed line around the orange ellipse. The base of the cratonic keel is marked by a dashed line, because the depth extent of the cratonic keel is uncertain.

importance of strong lateral velocity heterogeneity within the upper mantle and MTZ below the eastern U.S. We find no strong support for any of three previously proposed scenarios regarding possible vertical mantle flow geometries beneath the eastern U.S., including edge-driven convection (King, 2007; King & Anderson, 1998), hydrous upwelling (van der Lee et al., 2008), and a sinking delaminated or dripped cold lithospheric block from the lithosphere beneath the central WV/VA border (e.g., Biryol et al., 2016; Schmandt & Lin, 2014). We propose, instead, that a passive return hot upwelling induced by the neighboring sinking Farallon slab from the lower mantle (Piromallo et al., 2006) may exist beneath the eastern U.S. continental margin, which is consistent with the shallower 660-km interface and thinner MTZ beneath the southeastern part of the MAGIC profile. The hot upwelling will be hydrated as it rises through the hydrous MTZ fed by the dehydration of the Farallon slab at the top of the lower mantle, consistent with the elevated 410-km discontinuity beneath the coastal plain, because water has a much stronger effect on the phase transition pressure for 410-km discontinuity than that for 660-km discontinuity. The hydrous hot upwelling rising into the upper mantle may trigger dehydration melting atop 410-km discontinuity (Bercovici & Karato, 2003; Leahy & Bercovici, 2007). The melt may further ascend through the upper mantle ($S1_p/S1_s$) if it is positively buoyant and reach the base of the lithosphere (Byrnes et al., 2019; Evans et al., 2019; Long et al., 2021). We suggest that the coexistence of the hydration process within

MTZ and the hot upwelling return flow associated with the descending Farallon slab in the lower mantle may produce a hydro-thermal upwelling (Figure 4), which may play a major role in controlling the structures of the mid- and upper mantle beneath the eastern U.S. continental margin today.

Finally, we'd like to emphasize that the proposed hydro-thermal upwelling hypothesis does not rule out the possibility of other coexisting dynamic processes to contribute to the origin of the prominent slow velocity anomaly below central Appalachian Mountains ($S1_p$/$S1_s$ in Figure 2). Potentially, this slow velocity anomaly may be connected to the positively buoyant material in the deeper mantle beneath the Atlantic ocean, as indicated by the tomographic imaging from the recent deployment of the broadband ocean-bottom seismometers offshore at the eastern U.S. continental margin (Brunsvik et al., 2021).

## Data Availability Statement

Seismic waveform data used in this study include the United States National Seismic Network (network code US, https://doi.org/10.7914/SN/US), EarthScope USArray Transportable Array (network code TA, https://doi.org/10.7914/SN/TA), and the Mid-Atlantic Geophysical Integrative Collaboration (MAGIC) experiment (network code 7A, https://doi.org/10.7914/SN/7A_2013), which can be accessed via the IRIS Data Management Center (DMC) at https://ds.iris.edu/ds/nodes/dmc.

**Acknowledgments**
This research was partially supported by EarthScope and GeoPRISMS programs of the National Science Foundation through the Mid-Atlantic Geophysical Integrative Collaboration (MAGIC) project (Grants EAR-1250988, EAR-1251515, and EAR-1251329). We thank Lara Wagner, Ying Zhou, and Martin Chapman for helpful discussions on receiver function data processing. Shangxin Liu appreciates the extensive discussion with Alessandro Forte on mantle flow patterns beneath the eastern North America. The authors appreciate the efforts by the developers of Funclab (Eagar & Fouch, 2012; Porritt & Miller, 2018). Some figures were made with Generic Mapping Tools (Wessel & Smith, 1998). We thank Xuran Liang, Eva Golos, Barbara Romanowicz for sharing their seismic tomographic models, respectively. Utpal Kumar helped transfer the NASEM5 velocity model from A3d format to spatial domain. Brandon Schmandt provided the crustal velocity model used in the SL14 inversion for the 3D velocity corrections in this study. We further thank the Earth Model Collaboration (EMC) website (http://ds.iris.edu/ds/products/emc-earthmodels/) of the Incorporated Research Institutions for Seismology (IRIS) for hosting SL14, BBNAP19, and SAVANI-US seismic tomographic models (Trabant et al., 2012) and the original authors for providing these models to the website. The manuscript was improved by helpful comments from two anonymous reviewers and the editor, Daoyuan Sun.

## References

Aragon, J. C., Long, M. D., & Benoit, M. H. (2017). Lateral variations in SKS splitting across the magic array, central Appalachians. *Geochemistry, Geophysics, Geosystems*, *18*(11), 4136–4155. https://doi.org/10.1002/2017gc007169

Becker, T. W. (2012). On recent seismic tomography for the western United States. *Geochemistry, Geophysics, Geosystems*, *13*, Q01W10. https://doi.org/10.1029/2011GC003977

Benoit, M. H., Long, M. D., & King, S. D. (2013). Anomalously thin transition zone and apparently isotropic upper mantle beneath Bermuda: Evidence for upwelling. *Geochemistry, Geophysics, Geosystems*, *14*(10), 4282–4291. https://doi.org/10.1002/ggge.20277

Bercovici, D., & Karato, S. (2003). Whole-mantle convection and the transition-zone water filter. *Nature*, *425*(6953), 39–44. https://doi.org/10.1038/nature01918

Bina, C. R., & Helffrich, G. (1994). Phase transition Clapeyron slopes and transition zone seismic discontinuity topography. *Journal of Geophysical Research*, *99*(B8), 15853–15860. https://doi.org/10.1029/94jb00462

Biryol, C. B., Wagner, L. S., Fischer, K. M., & Hawman, R. B. (2016). Relationship between observed upper mantle structures and recent tectonic activity across the southeastern United States. *Journal of Geophysical Research: Solid Earth*, *121*(5), 3393–3414. https://doi.org/10.1002/2015jb012698

Boyce, A., Bastow, I. D., Golos, E. M., Rondenay, S., Burdick, S., & Van der Hilst, R. D. (2019). Variable modification of continental lithosphere during the Proterozoic Grenville orogeny: Evidence from teleseismic p-wave tomography. *Earth and Planetary Science Letters*, *525*, 115763. https://doi.org/10.1016/j.epsl.2019.115763

Brunsvik, B. R., Eilon, Z. C., & Lynner, C. (2021). Mantle structure and flow across the continent-ocean transition of the eastern North American margin: Anisotropic s-wave tomography. *Geochemistry, Geophysics, Geosystems*, *22*(12), e2021GC010084. https://doi.org/10.1029/2021gc010084

Byrnes, J. S., Bezada, M., Long, M. D., & Benoit, M. H. (2019). Thin lithosphere beneath the central Appalachian mountains: Constraints from seismic attenuation beneath the magic array. *Earth and Planetary Science Letters*, *519*, 297–307. https://doi.org/10.1016/j.epsl.2019.04.045

Clouzet, P., Masson, Y., & Romanowicz, B. (2018). Box tomography: First application to the imaging of upper-mantle shear velocity and radial anisotropy structure beneath the North American continent. *Geophysical Journal International*, *213*(3), 1849–1875. https://doi.org/10.1093/gji/ggy078

Conrad, C. P., & Molnar, P. (1997). The growth of Rayleigh-Taylor-type instabilities in the lithosphere for various rheological and density structures. *Geophysical Journal International*, *129*(1), 95–112. https://doi.org/10.1111/j.1365-246x.1997.tb00939.x

Cook, F. A., & Vasudevan, K. (2006). Reprocessing and enhanced interpretation of the initial cocorp southern Appalachians traverse. *Tectonophysics*, *420*(1–2), 161–174. https://doi.org/10.1016/j.tecto.2006.01.022

Dueker, K. G., & Sheehan, A. F. (1997). Mantle discontinuity structure from midpoint stacks of converted p to s waves across the Yellowstone hotspot track. *Journal of Geophysical Research*, *102*(B4), 8313–8327. https://doi.org/10.1029/96jb03857

Eagar, K. C., & Fouch, M. J. (2012). Funclab: A Matlab interactive toolbox for handling receiver function datasets. *Seismological Research Letters*, *83*(3), 596–603. https://doi.org/10.1785/gssrl.83.3.596

Evans, R. L., Benoit, M. H., Long, M. D., Elsenbeck, J., Ford, H. A., Zhu, J., & Garcia, X. (2019). Thin lithosphere beneath the central Appalachian mountains: A combined seismic and magnetotelluric study. *Earth and Planetary Science Letters*, *519*, 308–316. https://doi.org/10.1016/j.epsl.2019.04.046

Faccenna, C., Becker, T. W., Lallemand, S., Lagabrielle, Y., Funiciello, F., & Piromallo, C. (2010). Subduction-triggered magmatic pulses. A new class of plumes? *Earth and Planetary Science Letters*, *209*(1–2), 54–68. https://doi.org/10.1016/j.epsl.2010.08.012

Flanagan, M. P., & Shearer, P. M. (1998). Global mapping of topography on transition zone velocity discontinuities by stacking ss precursors. *Journal of Geophysical Research*, *103*(B2), 2673–2692. https://doi.org/10.1029/97jb03212

Forte, A. M., Mitrovica, J., Moucha, R., Simmons, N., & Grand, S. (2007). Descent of the ancient farallon slab drives localized mantle flow below the new Madrid seismic zone. *Geophysical Research Letters*, *34*(4), L04308. https://doi.org/10.1029/2006gl027895

Gao, S. S., & Liu, K. H. (2014). Mantle transition zone discontinuities beneath the contiguous United States. *Journal of Geophysical Research: Solid Earth*, *119*(8), 6452–6468. https://doi.org/10.1002/2014jb011253

Göğüş, O. H., & Pysklywec, R. N. (2008). Near-surface diagnostics of dripping or delaminating lithosphere. *Journal of Geophysical Research*, *113*(B11), B11404. https://doi.org/10.1029/2007jb005123

Golos, E., Fang, H., Yao, H., Zhang, H., Burdick, S., Vernon, F., et al. (2018). Shear wave tomography beneath the United States using a joint inversion of surface and body waves. *Journal of Geophysical Research: Solid Earth*, *123*(6), 5169–5189. https://doi.org/10.1029/2017jb014894

Grand, S. P. (2002). Mantle shear–wave tomography and the fate of subducted slabs. *Philosophical Transactions of the Royal Society of London, Series A: Mathematical, Physical and Engineering Sciences*, *360*(1800), 2475–2491. https://doi.org/10.1098/rsta.2002.1077

Grigné, C., & Labrosse, S. (2001). Effects of continents on Earth cooling: Thermal blanketing and depletion in radioactive elements. *Geophysical Research Letters*, *28*(14), 2707–2710. https://doi.org/10.1029/2000gl012475

Gu, Y., Dziewoński, A. M., & Agee, C. B. (1998). Global de-correlation of the topography of transition zone discontinuities. *Earth and Planetary Science Letters*, *157*(1–2), 57–67. https://doi.org/10.1016/s0012-821x(98)00027-2

Guo, Z., & Zhou, Y. (2021). Stagnant slabs and their return flows from finite-frequency tomography of the 410-km and 660-km discontinuities. *Journal of Geophysical Research: Solid Earth*, *126*(5), e2020JB021099. https://doi.org/10.1029/2020jb021099

Higo, Y., Inoue, T., Irifune, T., & Yurimoto, H. (2001). Effect of water on the spinel-postspinel transformation in $Mg_2SiO_4$. *Geophysical Research Letters*, *28*(18), 3505–3508. https://doi.org/10.1029/2001gl013194

Keifer, I., & Dueker, K. (2019). Testing the hypothesis that temperature modulates 410 and 660 discontinuity topography beneath the eastern United States. *Earth and Planetary Science Letters*, *524*, 115723. https://doi.org/10.1016/j.epsl.2019.115723

Kennett, B., & Engdahl, E. (1991). Traveltimes for global earthquake location and phase identification. *Geophysical Journal International*, *105*(2), 429–465. https://doi.org/10.1111/j.1365-246x.1991.tb06724.x

Kennett, B. L. N., Engdahl, E. R., & Buland, R. (1995). Constraints on seismic velocities in the Earth from travel times. *Geophysical Journal International*, *122*(1), 108–124. https://doi.org/10.1111/j.1365-246x.1995.tb03540.x

Khan, A., Connolly, J., & Olsen, N. (2006). Constraining the composition and thermal state of the mantle beneath Europe from inversion of long-period electromagnetic sounding data. *Journal of Geophysical Research*, *111*(B10), B10102. https://doi.org/10.1029/2006jb004270

King, S. D. (2007). Hotspots and edge-driven convection. *Geology*, *35*(3), 223–226. https://doi.org/10.1130/g23291a.1

King, S. D., & Anderson, D. L. (1998). Edge-driven convection. *Earth and Planetary Science Letters*, *160*(3–4), 289–296. https://doi.org/10.1016/s0012-821x(98)00089-2

Komabayashi, T., Omori, S., & Maruyama, S. (2004). Petrogenetic grid in the system MgO-$SiO_2$-$H_2O$ up to 30 gpa, 1600 c: Applications to hydrous peridotite subducting into the Earth's deep interior. *Journal of Geophysical Research*, *109*(B3), B03206. https://doi.org/10.1029/2003jb002651

Langston, C. A. (1977). Corvallis, Oregon, crustal and upper mantle receiver structure from teleseismic p and s waves. *Bulletin of the Seismological Society of America*, *67*(3), 713–724. https://doi.org/10.1785/bssa0670030713

Lawrence, J., & Shearer, P. (2006). A global study of transition zone thickness using receiver functions. *Journal of Geophysical Research*, *111*(B6), B06307. https://doi.org/10.1029/2005JB003973

Leahy, G. M., & Bercovici, D. (2007). On the dynamics of a hydrous melt layer above the transition zone. *Journal of Geophysical Research*, *112*(B7), B07401. https://doi.org/10.1029/2006jb004631

Liang, X., Zhao, D., Hua, Y., & Xu, Y.-G. (2022). Seismic anisotropy tomography and mantle dynamics of central-eastern USA. *Journal of Geophysical Research: Solid Earth*, *127*(12), e2022JB025484. https://doi.org/10.1029/2022jb025484

Ligorria, J. P., & Ammon, C. J. (1999). Iterative deconvolution and receiver-function estimation. *Bulletin of the Seismological Society of America*, *89*(5), 1395–1400. https://doi.org/10.1785/bssa0890051395

Long, M. D., Benoit, M. H., Aragon, J. C., & King, S. D. (2019). Seismic imaging of mid-crustal structure beneath central and eastern North America: Possibly the elusive Grenville deformation? *Geology*, *47*(4), 371–374. https://doi.org/10.1130/g46077.1

Long, M. D., Benoit, M. H., Chapman, M. C., & King, S. D. (2010). Upper mantle anisotropy and transition zone thickness beneath south-eastern North America and implications for mantle dynamics. *Geochemistry, Geophysics, Geosystems*, *11*(10), Q10012. https://doi.org/10.1029/2010gc003247

Long, M. D., Benoit, M. H., Evans, R. L., Aragon, J. C., & Elsenbeck, J. (2020). The magic experiment: A combined seismic and magnetotelluric deployment to investigate the structure, dynamics, and evolution of the central appalachians. *Seismological Research Letters*, *91*(5), 2960–2975. https://doi.org/10.1785/0220200150

Long, M. D., Wagner, L. S., King, S. D., Evans, R. L., Mazza, S. E., Byrnes, J. S., et al. (2021). Evaluating models for lithospheric loss and intraplate volcanism beneath the central Appalachian Mountains. *Journal of Geophysical Research: Solid Earth*, *126*(10), e2021JB022571. https://doi.org/10.1029/2021jb022571

Maguire, R., Ritsema, J., & Goes, S. (2018). Evidence of subduction-related thermal and compositional heterogeneity below the United States from transition zone receiver functions. *Geophysical Research Letters*, *45*(17), 8913–8922. https://doi.org/10.1029/2018gl078378

Mazza, S. E., Gazel, E., Johnson, E. A., Kunk, M. J., McAleer, R., Spotila, J. A., et al. (2014). Volcanoes of the passive margin: The youngest magmatic event in eastern North America. *Geology*, *42*(6), 483–486. https://doi.org/10.1130/g35407.1

Nance, R. D., Murphy, J. B., & Santosh, M. (2014). The supercontinent cycle: A retrospective essay. *Gondwana Research*, *25*(1), 4–29. https://doi.org/10.1016/j.gr.2012.12.026

Neely, J. S., Stein, S., Merino, M., & Adams, J. (2018). Have we seen the largest earthquakes in eastern North America? *Physics of the Earth and Planetary Interiors*, *284*, 17–27. https://doi.org/10.1016/j.pepi.2018.09.005

Ohtani, E., & Litasov, K. (2006). The effect of water on mantle phase transitions. *Reviews in Mineralogy and Geochemistry*, *62*(1), 397–420. https://doi.org/10.2138/rmg.2006.62.17

Piromallo, P., Becker, T. W., Funiciello, F., & Faccenna, C. (2006). Three-dimensional instantaneous mantle flow induced by subduction. *Geophysical Research Letters*, *33*(8), L08304. https://doi.org/10.1029/2005GL025390

Porritt, R. W., Becker, T. W., Boschi, L., & Auer, L. (2021). Multiscale, radially anisotropic shear wave imaging of the mantle underneath the contiguous United States through joint inversion of USArray and global data sets. *Geophysical Journal International*, *226*(3), 1730–1746. https://doi.org/10.1093/gji/ggab185

Porritt, R. W., & Miller, M. S. (2018). Updates to FuncLab, a Matlab based GUI for handling receiver functions. *Computers & Geosciences*, *111*, 260–271. https://doi.org/10.1016/j.cageo.2017.11.022

Pratt, T. L., Horton, J. W., Spears, D. B., Gilmer, A. K., & McNamara, D. E. (2015). The 2011 Virginia mw 5.8 earthquake: Insights from seismic reflection imaging into the influence of older structures on eastern us seismicity. *Geological Society of America Special Paper*, *509*, 285–294.

Rowley, D. B., Forte, A. M., Moucha, R., Mitrovica, J. X., Simmons, N. A., & Grand, S. P. (2013). Dynamic topography change of the eastern United States since 3 million years ago. *Science*, *340*(6140), 1560–1563. https://doi.org/10.1126/science.1229180

Schmandt, B., & Lin, F.-C. (2014). P and S wave tomography of the mantle beneath the United States. *Geophysical Research Letters*, *41*(18), 6342–6349. https://doi.org/10.1002/2014gl061231

Schmandt, B., Lin, F.-C., & Karlstrom, K. E. (2015). Distinct crustal isostasy trends east and west of the Rocky Mountain Front. *Geophysical Research Letters*, *42*(23), 10–290. https://doi.org/10.1002/2015gl066593

Shearer, P. M. (2000). Upper mantle seismic discontinuities. *Geophysical monograph-American Geophysical Union*, *117*, 115–132.

Shen, W., & Ritzwoller, M. H. (2016). Crustal and uppermost mantle structure beneath the United States. *Journal of Geophysical Research: Solid Earth*, *121*(6), 4306–4342. https://doi.org/10.1002/2016jb012887

Smyth, J. R., & Frost, D. J. (2002). The effect of water on the 410-km discontinuity: An experimental study. *Geophysical Research Letters*, *29*(10), 123–131. https://doi.org/10.1029/2001gl014418

Trabant, C., Hutko, A. R., Bahavar, M., Karstens, R., Ahern, T., & Aster, R. (2012). Data products at the IRIS DMC: Stepping stones for research and other applications. *Seismological Research Letters*, *83*(5), 846–854. https://doi.org/10.1785/0220120032

van der Lee, S., Regenauer-Lieb, K., & Yuen, D. A. (2008). The role of water in connecting past and future episodes of subduction. *Earth and Planetary Science Letters*, *273*(1–2), 15–27. https://doi.org/10.1016/j.epsl.2008.04.041

Verhoeven, O., Mocquet, A., Vacher, P., Rivoldini, A., Menvielle, M., Arrial, P.-A., et al. (2009). Constraints on thermal state and composition of the Earth's lower mantle from electromagnetic impedances and seismic data. *Journal of Geophysical Research*, *114*(B3), B03302. https://doi.org/10.1029/2008jb005678

Vinnik, L. (1977). Detection of waves converted from P to SV in the mantle. *Physics of the Earth and Planetary Interiors*, *15*(1), 39–45. https://doi.org/10.1016/0031-9201(77)90008-5

Wagner, L. S., Fischer, K. M., Hawman, R., Hopper, E., & Howell, D. (2018). The relative roles of inheritance and long-term passive margin lithospheric evolution on the modern structure and tectonic activity in the southeastern United States. *Geosphere*, *14*(4), 1385–1410. https://doi.org/10.1130/ges01593.1

Wang, X.-C., Wilde, S. A., Li, Q.-L., & Yang, Y.-N. (2015). Continental flood basalts derived from the hydrous mantle transition zone. *Nature Communications*, *6*(1), 1–9. https://doi.org/10.1038/ncomms8700

Wang, Y., & Pavlis, G. L. (2016). Roughness of the mantle transition zone discontinuities revealed by high-resolution wavefield imaging. *Journal of Geophysical Research: Solid Earth*, *121*(9), 6757–6778. https://doi.org/10.1002/2016jb013205

Wei, S. S., & Shearer, P. M. (2017). A sporadic low-velocity layer atop the 410 km discontinuity beneath the Pacific Ocean. *Journal of Geophysical Research: Solid Earth*, *122*(7), 5144–5159. https://doi.org/10.1002/2017jb014100

Wessel, P., & Smith, W. H. (1998). New, improved version of generic mapping tools released. *Eos, Transactions American Geophysical Union*, *79*(47), 579. https://doi.org/10.1029/98eo00426

Wolin, E., Stein, S., Pazzaglia, F., Meltzer, A., Kafka, A., & Berti, C. (2012). Mineral, Virginia, earthquake illustrates seismicity of a passive-aggressive margin. *Geophysical Research Letters*, *39*(2), L02305. https://doi.org/10.1029/2011gl050310

Wood, B. (1995). The effect of $H_2O$ on the 410-kilometer seismic discontinuity. *Science*, *268*(5207), 74–76. https://doi.org/10.1126/science.268.5207.74

Zhou, Y. (2018). Anomalous mantle transition zone beneath the Yellowstone hotspot track. *Nature Geoscience*, *11*(6), 449–453. https://doi.org/10.1038/s41561-018-0126-4